Earth and Planetary Science Letters 300 (2010) 101–111

Contents lists available at ScienceDirect

Earth and Planetary Science Letters

journal homepage: www.elsevier.com/locate/epsl

Isotopic evidence for an anomalously low oceanic sulfate concentration following end-Permian mass extinction

Genming Luo [a,b,c], Lee R. Kump [c,*], Yongbiao Wang [a], Jinnan Tong [a], Michael A. Arthur [c], Hao Yang [a], Junhua Huang [b], Hongfu Yin [b], Shucheng Xie [a,*]

[a] Key Laboratory of Biogeology and Environmental Geology of Ministry of Education, China University of Geosciences, Wuhan 430074, People's Republic of China
[b] State Key Laboratory of Geological Processes and Mineral Resources, China University of Geosciences, Wuhan 430074, People's Republic of China
[c] Department of Geosciences and Earth System Science Center, The Pennsylvania State University, University Park, PA 16802, USA

ARTICLE INFO

Article history:
Received 6 May 2010
Received in revised form 19 September 2010
Accepted 26 September 2010
Available online 20 October 2010

Editor: M.L. Delaney

Keywords:
oceanic sulfate concentration
carbon isotopes
sulfur isotopes
microbialite
Permian–Triassic transition
South China

ABSTRACT

The cataclysmic end-Permian mass extinction was immediately followed by a global expansion of microbial ecosystems, as demonstrated by widespread microbialite sequences (disaster facies) in shallow water settings. Here we present high-resolution carbonate carbon ($\delta^{13}C_{carb}$) and carbonate-associated sulfate–sulfur isotope ($\delta^{34}S_{CAS}$) records from the microbialite in the Cili Permian–Triassic (P–Tr) section in South China. A stepwise decline in $\delta^{13}C_{carb}$ begins in the underlying skeletal limestone, predating the main oceanic mass extinction and the first appearance of microbialite, and reaches its nadir in the upper part of the microbialite layer. The corresponding $\delta^{34}S_{CAS}$, in the range of 17.4‰ to 27.4‰, is relatively stable in the underlying skeletal limestone, and increases gradually from 2 m below the microbialite rising to a peak at the base of the microbialite. Two episodes of positive and negative shifts occurred within the microbialite layer, and exhibit a remarkable co-variance of sulfur and carbon isotope composition. The large amplitude of the variation in $\delta^{34}S_{CAS}$, as high as 7‰ per 100 kiloyears, suggests a small oceanic sulfate reservoir size at this time. Furthermore, the $\delta^{13}C_{carb}$ and $\delta^{34}S_{CAS}$ records co-vary without phase lag throughout the microbialite interval, implying a marine-driven C cycle in an anoxic ocean with anomalously low oceanic sulfate concentrations. On the basis of a non-steady-state box model, we argue that the oceanic sulfate concentration may have fallen to less than 15%, perhaps as low as 3%, of that in the modern oceans. Low oceanic sulfate concentration likely was the consequence of evaporite deposition and widespread anoxic/sulfidic conditions prior to the main mass extinction. By promoting methanogenesis and a build-up of atmospheric CH_4 and CO_2, low oceanic sulfate may have intensified global warming, exacerbating the inimical environmental conditions of the latest Permian.

1. Introduction

The most severe extinction since the advent of animal life on Earth occurred at the end of the Permian Period (Erwin, 2006; Ward et al., 2005). Several scenarios have been advanced for the mechanism(s) that induced this extinction (Basu et al., 2003; Knoll et al., 2007; Kump et al., 2005; Reichow et al., 2009; Svensen et al., in press; Wignall and Hallam, 1993; Yin et al., 2007). The two commonly considered mechanisms, volcanism and oceanic anoxia/euxinia, have the potential to severely disrupt the global carbon and sulfur cycles, and could thus explain the large fluctuations in the carbon and sulfur isotope composition of the ocean observed in rocks of latest Permian and early Triassic age (Algeo et al., 2007; Baud et al., 1989; Cao et al., 2002; Corsetti et al., 2005; Dolenec et al., 2004; Gorjan et al., 2007; Holser et al., 1989; Kaiho et al., 2001; Korte and Kozur, 2010; Korte et al., 2010; Luo et al., 2010; Magaritz et al., 1988; Newton et al., 2004; Payne et al., 2004; Riccardi et al., 2006; Richoz et al., 2010; Xie et al., 2007). Previous work mainly focused on the mechanisms that caused these fluctuations in carbon or sulfur isotope composition and their relations to the mass extinction event. Large fluctuations in $\delta^{13}C_{carb}$ have been interpreted as an indication of environmental instability (Payne and Kump, 2007; Payne et al., 2004). However, there has been less effort expended on investigating coupling of the C and S cycles during the event, especially in the environmental aftermath of the extinction.

Oceanic sulfate is an important bridge linking the carbon and sulfur cycles through bacterial sulfate reduction. Somewhat lower-than-modern oceanic sulfate concentrations (~20 mM) have been estimated for the Permian and Triassic oceans based on the brine inclusion in halite (Horita et al., 2002; Kovalevich et al., 1998; Kovalevych et al., 2002; Lowenstein et al., 2005). However, there is a lack of evaporite data from the P–Tr crisis interval and from much of

* Corresponding authors.
E-mail addresses: lkump@psu.edu (L.R. Kump), xiecug@163.com (S. Xie).

0012-821X/$ – see front matter © 2010 Elsevier B.V. All rights reserved.
doi:10.1016/j.epsl.2010.09.041

the Early Triassic, which impedes the evaluation of the oceanic sulfate concentration at this time interval based on this method. Holser and Magaritz (1987) invoked a smaller oceanic sulfate reservoir to explain rapid fluctuations in $\delta^{34}S$ in the Late Permian and Early Triassic ocean. Marenco et al. (2008) also noted that the oceanic sulfate concentration should be considerably lower than that of today in order to maintain an observed surface to deep gradient in oceanic sulfate $\delta^{34}S$ for millions of years. However, these authors neither treated the problem quantitatively nor discussed their implications for the oceans and links to the extinction.

The extinction, in shallow water settings, was immediately followed by a global expansion of microbial ecosystems as demonstrated by widespread microbialite sequences (disaster facies) (Baud et al., 2007; Pruss et al., 2006), the base of which is proposed to represent the maximum extinction horizon (Krull et al., 2004). This contact, readily distinguishable in South China as well as in the Tethys region, thus provides a stratigraphic tool to correlate the mass extinction with various geochemical parameters in sections characterized by the occurrence of microbialite. The transition from skeletal limestone to carbonate microbialite at the location of the present study (Cili, South China) is conformable, allowing us to establish a continuous record of $\delta^{13}C_{carb}$ and $\delta^{34}S_{CAS}$ through the extinction event and its aftermath.

In the present study, we have analyzed both the $\delta^{13}C_{carb}$ and $\delta^{34}S_{CAS}$ on the same samples at high resolution, and evaluated the possibility of diagenetic artifacts using a combination of oxygen isotope and elemental analysis. Box modeling is used to quantitatively evaluate the nature of the coupling of C and S cycles and requisite variations in oceanic sulfate concentration during the P–Tr transition. We then consider how severely depressed oceanic sulfate concentrations may have exacerbated environmental stress in the post-extinction interval.

2. Geological background

2.1. Paleogeography

During the P–Tr transition, the South China Block was located near the equator in the Eastern Paleo-Tethys Ocean (Fig. 1A). The studied Cili section crops out in the county of Cili, about 300 km northwest of Changsha, the capital city of the Hunan Province in South China, and about 800 km southwest of the Global Stratotype Section and Point (GSSP) section, Meishan D section in Zhejiang Province. From the Late Permian to the Early Triassic, the study area was a carbonate platform, known as the Jiangnan carbonate platform (Feng et al., 1997). The Cili section was located in the middle part of the platform and was connected to the open ocean to the northwest (Fig. 1B).

2.2. Biostratigraphy

Skeletal limestone, microbialite and interbeds of thinly bedded micritic limestone and oolitic limestone can be divided easily in ascending order in the Cili section. The skeletal limestone below the base of the microbialite contains abundant fusulinids, non-fusulinid foraminifera, and algae, including the index fossils of the end-Permian *Palaeofusulina–Colaniella* zone (Wang et al., 2009). A 6.7 m thick microbialite overlies the skeletal limestone and is composed of stromatolites and thrombolites. On the basis of our previous investigation (Wang et al., 2009), the first appearance of the index fossil for the P–Tr boundary, *Hindeodus parvus*, occurs at about 5.7 m above the base of the microbialite at our section. The lower part of the microbialite corresponds to the *Neogondolella meishanensis* and *H. changxingensis* conodont zones or beds 25 to 27b at the GSSP section (Jiang et al., 2007). The subdivision of the microbialite interval is in accordance with that in other sections in South China where the lower part of the microbialite is proposed to be the end-Permian and the *H. parvus* zone begins somewhere within the upper part of the microbialite (Lehrmann et al., 2003; Wang et al., 2005; Yang et al., 2006). Thinly bedded limestones and oolitic limestones are deposited on top of the microbialite. The *Isarcicella staeschei* zone is found in the thinly bedded limestone, about 13.6 m above the base of the microbialite (Wang et al., 2009). The *Isarcicella staeschei* zone, as a newly differentiated zone from the lower part of *I. isracica* zone from Meishan (Jiang et al., 2007), can also be identified in the Siusi and Bulla sections in western Tethys Ocean (Farabegoli et al., 2007).

3. Materials and methods

Large fresh samples (about 3–4 kg) were collected from the skeletal limestone, microbialite and the overlying oolite and thin-bedded carbonate at Cili section. Weathered surfaces and large post-depositional veins were cut off during the field collection.

3.1. Carbonate carbon isotope composition

Each large sample was cut into small pieces in the laboratory. Fresh chips were chosen and crushed to less than 100 mesh. In order to determine whether the carbon isotope compositions were different in micrite and spar in the same sample, these two fractions in several samples were separated for both $\delta^{13}C_{carb}$ and $\delta^{18}O_{carb}$ investigation. The carbonate carbon isotope compositions were determined according to McCrea (1950). Under vacuum, the sample powder was reacted offline with 100% H_3PO_4 for 24 h at 25 °C. The carbon isotope composition of the generated CO_2 was measured on a Finnigan MAT 251 mass spectrometer. All isotope data are reported as per mil (‰) relative to Vienna Pee Dee belemnite (VPDB) standard. The analytical precision is better than ±0.1‰ for $\delta^{13}C$ and ±0.3‰ for $\delta^{18}O$ based on duplicate analyses.

3.2. CAS extraction and sulfur isotope composition

Samples with few pyrite grains, as determined by thin section examination, were selected for CAS extraction. Marenco et al. (2007) and Mazumdar et al. (2008) showed that the presence of oxygen would not affect the CAS-sulfur isotope value when pyrite concentration is low (<1%). Our samples selected for this measurement have pyrite content less than 0.4%, and meet this requirement. The procedure for CAS extraction follows Newton et al. (2004) and Riccardi et al. (2006). 150 g sample powder (<100 mesh) was weighed and leached in 10% NaCl solution for 24 h, and then washed three times with deionized water to remove soluble sulfate. Leached powder was re-leached in 5.25% NaClO solution for other 24 h, and washed three times with deionized water to remove organic sulfur and sulfide minerals. The cleaned and rinsed powder was then reacted with 6 M HCl in contact with air. After carbonate was quantitatively dissolved, the solution was passed through a 1 μm filter paper and the residue was collected for organic carbon isotope analysis. 10–20 mL saturated $BaCl_2$ solution was added into the liquid to precipitate quantitatively the sulfate present in the solution as $BaSO_4$. The solution was heated for about 1 h and set aside for 12 h. The barite precipitate was collected the following day. Approximately 15 mg of $BaSO_4$ sample was mixed with V_2O_5 (100 mg) and SiO_2 (100 mg) and combusted in the presence of copper turnings (100–150 mg) under vacuum for quantitative conversion to sulfur dioxide (SO_2). The collected SO_2 was measured on a Finnigan MAT 251 mass spectrometer. All isotope data are reported as per mil (‰) relative to the international standard Vienna Canyon Diablo Troilite (VCDT). The analytical precision is better than ±0.2‰.

3.3. Element concentration

Fresh samples were crashed to less than 200 mesh for elemental analysis. The measurement of strontium (Sr) and manganese (Mn)

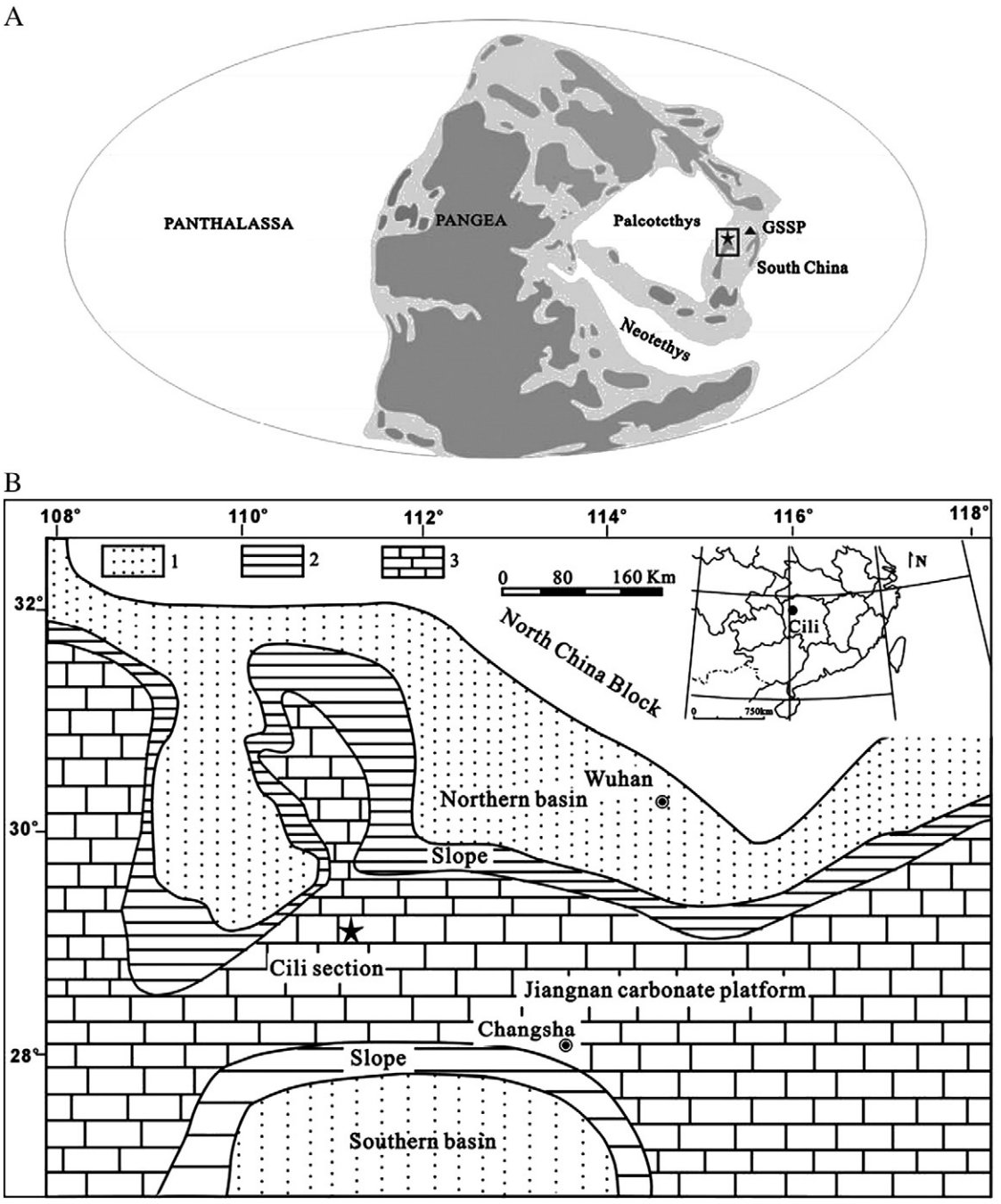

Fig. 1. A: Paleogeography of the Paleo-Tethys Ocean and location of the South China Block. The square represents the study area. GSSP: Global Stratotype Section and Point, Meishan D section in Zhejiang Province. B: Sedimentary facies of middle part of the South China Block (after Feng et al., 1997). The star represents the location of the Cili section. 1, deep basin; 2, platform margin or slope; 3, carbonate platform.

elemental concentration was carried out in the geochemical laboratory at the China University of Geosciences according to the methods of Liu et al. (2008). ICP-MS was used to analyze the Sr and Mn concentration with an average analytical uncertainty of ±5 wt.%. Fe was measured by ICP-AES with an average analytical uncertainty of ± 10 wt.%.

4. Results

4.1. Carbonate carbon isotope composition

The $\delta^{13}C_{carb}$ of the studied interval ranges from +4.5‰ to −0.8‰ (Fig. 2B), and the trend toward lower values is not accompanied by a downward trend in $\delta^{18}O_{carb}$ as might be expected if this trend was largely the result of meteoric diagenesis (Fig. 2A). In fact, the interval of particular interest, the microbialite, is notably depleted in ^{13}C but enriched in ^{18}O.

A stepwise negative $\delta^{13}C_{carb}$ excursion starts in the underlying skeletal limestone and ends in the lower part of the *Isarcicella staeschei* conodont zone. A small increase in $\delta^{13}C_{carb}$ is followed again by a decline near the top of our studied section (Fig. 2B). High-resolution $\delta^{13}C_{carb}$ around the mass extinction boundary shows a positive shift, about 1‰, directly after the extinction event (Fig. 2D).

Within the microbialite layer itself one can recognize three progressive cycles, I to III, characterized by a rapid negative shift in $\delta^{13}C_{carb}$ followed by a small and relatively gradual positive excursion

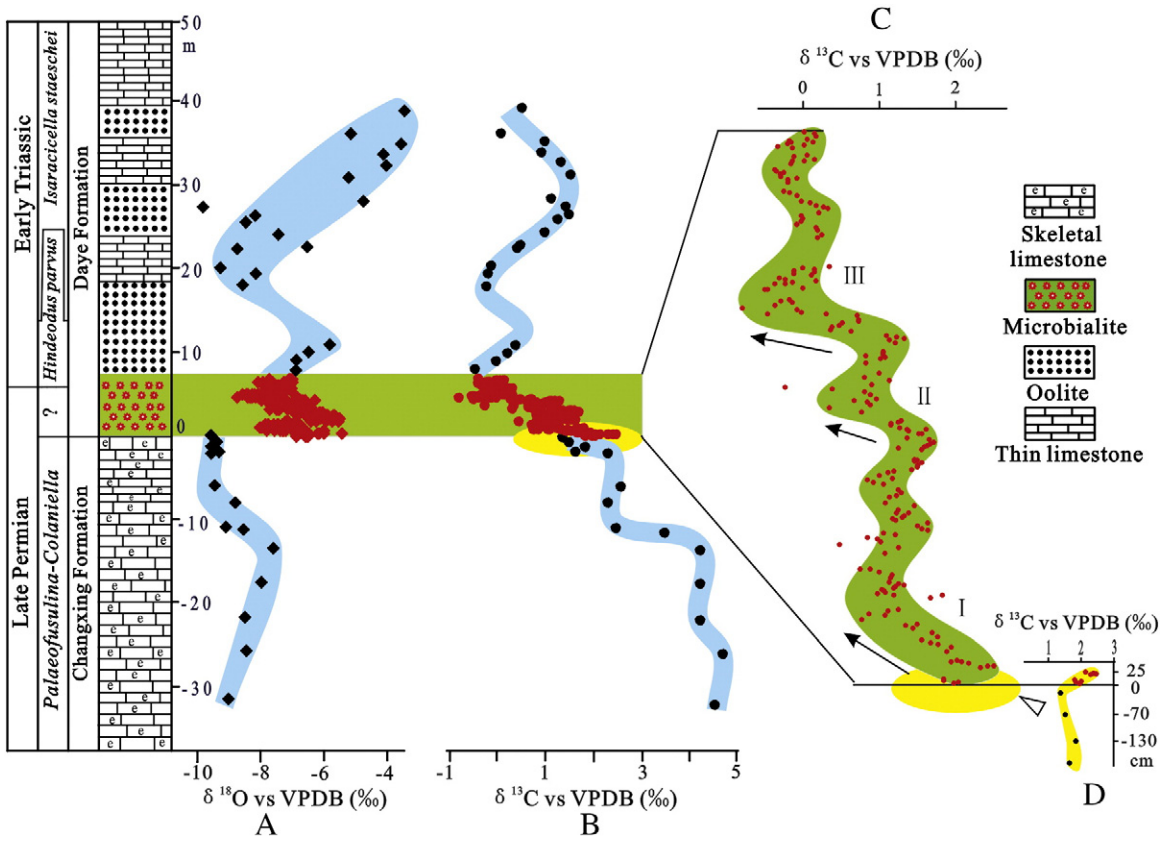

Fig. 2. Profiles of the high-resolution record of marine carbonate carbon and oxygen isotope compositions (relative to VPDB-Vienna Peedee belemnite) at Cili Section, Hunan Province, South China. (A) Variation of the corresponding carbonate oxygen isotope composition from the end of Late Permian to the earliest Triassic. (B) Variation of the carbonate carbon isotope composition from the end of Late Permian to the earliest Triassic. (C) Enlargement of the high-resolution variation of the carbon isotope composition in the microbialite layer. I, II and III represent the three evolution phases of the carbon isotope composition. (D) Enlargement of the carbon isotope composition during the mass extinction boundary. Black and red points represent carbon isotope composition before (skeletal limestone) and after (microbialite) the mass extinction, respectively. Biostratigraphy after Wang et al. (2009).

(Fig. 2C). In cycle I, the $\delta^{13}C_{carb}$ declines from >2‰ to <1‰ in the interval from 0 cm to 80 cm above the base of the microbialite, followed by a gradual positive excursion to about 1.5‰ in the interval from 80 to 310 cm. The intervals of the negative and positive shift in $\delta^{13}C_{carb}$ of cycle II are from 310 cm to 360 cm and from 360 cm to 420 cm, respectively. Cycle III documents a sharp negative shift in $\delta^{13}C_{carb}$, from 1.3‰ to −0.5‰ in the interval from 420 cm to 480 cm above the base of the microbialite.

4.2. CAS-sulfur isotope composition

$\delta^{34}S_{CAS}$ ranges from +17‰ to +27‰ (vs VCDT) in the interval from the underlying skeletal limestone to the overlying thinly bedded limestone (Fig. 3A, B). In the lower part of the skeletal limestone (from 22 m to 6 m below the base of the microbialite), the $\delta^{34}S_{CAS}$ was relatively stable, varying around +24‰. $\delta^{34}S_{CAS}$ then declined slightly, from +24.0‰ to +21.0‰ (Fig. 3A). Three ensuing episodes of positive shift in $\delta^{34}S_{CAS}$ are present in the Cili section. The first episode starts at 2 m below the base of the microbialite, and continues well into the lower part of the microbialite (40 cm above the base of the microbialite). The second episode of positive shift in $\delta^{34}S_{CAS}$ occurs in the microbialite layer (about 1 m above the base of the microbialite) and is followed by a high positive $\delta^{34}S_{CAS}$ plateau (Fig. 3B). The beginning of the third episode is present in the uppermost microbialite and continues into the overlying thinly bedded limestone (Fig. 3B). The intervening two episodes of negative shift in $\delta^{34}S_{CAS}$ are characterized by large amplitude, as large as 10‰ (Fig. 3B).

4.3. Elemental concentration

The Sr concentrations of the analyzed samples range from 80 to 135 ppm, with the corresponding Mn concentrations ranging from 82 to 196 ppm. The underlying skeletal limestones have a relatively higher Sr (212 ppm, n = 10) and lower Mn concentration (29 ppm, n = 10) compared with that in the microbialites, which are 126 ppm and 94 ppm, respectively. However, all the samples are characterized by low Mn/Sr ratios in the range of 0.6 to 2. The total Fe concentrations of all the samples range from 40 ppm to 2600 ppm with higher values in the microbialite.

5. Discussion

5.1. Evaluation of diagenetic overprinting

Stromatolite and thrombolite are the two main types of microbialites at the Cili section. Thin sections show that the stromatolitic horizons are primarily composed of micritic calcite with minor dolomite, whereas the thrombolites are composed of spar and micritic calcite with minor dolomite. Two lines of evidence suggest the spar was formed during early diagenesis: 1) well-preserved fossils occur within the spar (Lehrmann et al., 2003; Wang et al., 2005) suggesting that the spar was a pore-filling early diagenetic cement; 2) there is no systematic distinct difference in the carbon and oxygen isotope values between micrite and spar in the thrombolite (Fig. 4; see also Mu et al., 2009). The second line of evidence suggests that the $\delta^{13}C_{carb}$ of the bulk carbonate likely represents the carbon isotope composition of the coeval ocean.

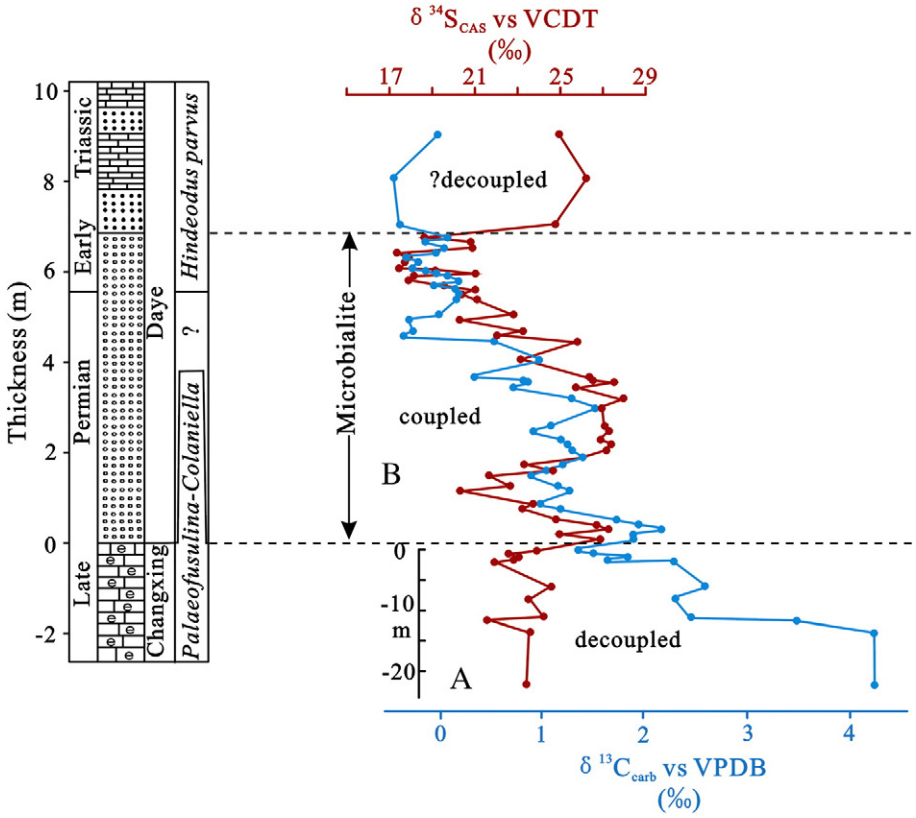

Fig. 3. Profiles of $\delta^{13}C_{carb}$ and $\delta^{34}S_{CAS}$ at the Cili Section in Hunan Province, South China. (A) Uncoupled C and S isotope variations in the pre-extinction skeletal limestone. (B) Coupled C and S isotope variations in the latest Permian to earliest Triassic microbialite. The carbon isotope composition is the mean value of the measured samples in the interval of the corresponding $\delta^{34}S_{CAS}$. Note the different thickness scales of Fig. 3A and B.

Relatively low ratios of Mn/Sr (all of the samples <2) fall well below the exclusion threshold of Kaufman and Knoll (1995), who concluded that primary $\delta^{13}C$ was retained when Mn/Sr<10 for Neoproterozoic carbonate rocks. Preservation of primary $\delta^{13}C_{carb}$ is also evidenced by relatively enriched $\delta^{18}O$ (Fig. 2A) in comparison to other horizons above and below the boundary interval, and there is no correlation between $\delta^{13}C$ and $\delta^{18}O$ ($R^2 = 0.021$) overall. Within the stromatolite/thrombolite interval there is a weak negative correlation ($R^2 = 0.25$) between Mn/Sr and $\delta^{18}O$ that could suggest modest meteoric diagenesis that increased Mn relative to Sr in carbonate cements while driving bulk rock $\delta^{18}O$ values more negative (Fig. 5). There is no relationship, however, between $\delta^{13}C_{carb}$ values and Mn/Sr, nor is there a relationship between Mn/Sr and CAS concentration or $\delta^{34}S_{CAS}$ values. Thus, we hold that primary carbon and sulfur isotope values were retained during diagenesis.

Few pyrite grains could be found in the thin sections of our samples analyzed here. The iron concentration, with an average of 1800 ppm in the microbialite layer, further suggests that pyrite, if present, represents less than 0.4% by weight in each sample. Uncorrelated $\delta^{34}S_{CAS}$ and CAS concentration variations ($R^2 = 0.001$) suggest that no significant pyrite oxidation occurred during preparation, which is also evidenced by uncorrelated Fe concentration and $\delta^{34}S_{CAS}$ (Fig. 5). So our $\delta^{34}S_{CAS}$ data likely have retained the primary oceanic sulfate sulfur isotope composition. Furthermore, consistent variations in $\delta^{13}C_{carb}$ and $\delta^{34}S_{CAS}$ that resemble $\delta^{13}C_{carb}$ and $\delta^{34}S_{CAS}$ variations at the coeval P–Tr sections in other locations (see below) also suggest that the Cili record does indeed reflect global (or at least Tethyan-wide) phenomena.

5.2. Correlation of $\delta^{13}C_{carb}$ and $\delta^{34}S_{CAS}$ during the P–Tr transition with other sections

5.2.1. $\delta^{13}C_{carb}$

$\delta^{13}C_{carb}$ records during the P–Tr transition are widely documented. Holser et al. (1989) was the first to identify two episodes of negative shift in $\delta^{13}C_{carb}$ during the P–Tr transition in Austria, and these were

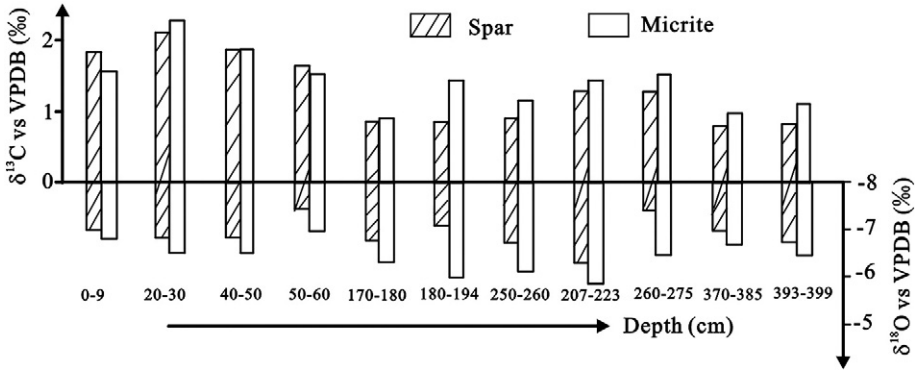

Fig. 4. Carbon and oxygen isotope composition of the micrite and spar in the same sample from different depths.

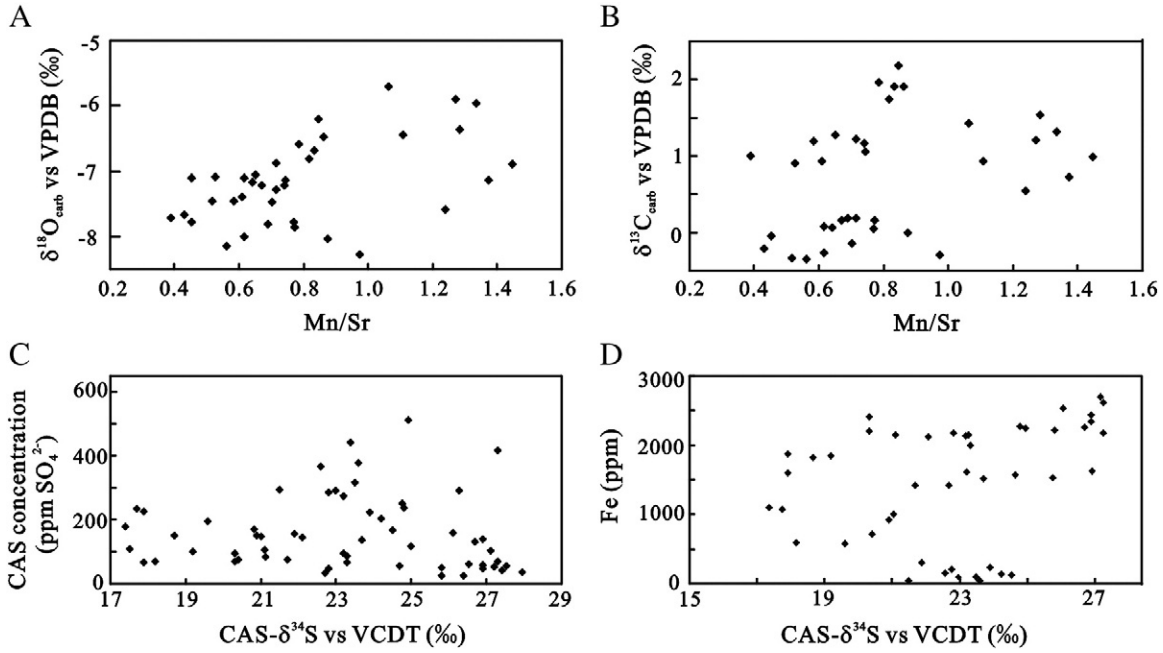

Fig. 5. Elemental and stable isotope analysis for the Cili section. A: cross-plot between oxygen isotopes for the carbonates and Mn/Sr ratio in the microbialite layer. B: The carbon isotopes for the carbonate compared the Mn/Sr ratio in the microbialite layer. C: $\delta^{34}S_{CAS}$ vs CAS concentration described as ppm of SO_4^{2-}. D: Comparison between $\delta^{34}S_{CAS}$ and the total Fe concentration.

later confirmed at other localities including the GSSP (Korte et al., 2004b; Xie et al., 2007). Based on conodont biostratigraphy, the two episodes of negative shift in $\delta^{13}C_{carb}$ presented in the Cili section are comparable with those previously reported (Fig. 6A). The gradual negative shift in $\delta^{13}C_{carb}$ predating the main oceanic mass extinction in the Cili section is also found in other sections (Holser et al., 1989; Korte et al., 2004b; Luo et al., 2010; Payne et al., 2004; Richoz et al., 2010; Xie et al., 2007) and is widely accepted now (Korte & Kozur, 2010). The slight positive shift in $\delta^{13}C_{carb}$ directly after the main oceanic mass extinction is different from previous suggestions that sharp negative shift in $\delta^{13}C_{carb}$ occurred immediately after the main oceanic mass extinction (Krull et al., 2004). It is interesting to note that this coeval slight positive shift in $\delta^{13}C_{carb}$ is reported recently in Oman and Iran (Korte & Kozur, 2010; Richoz et al., 2010). It is presently impossible, however, to correlate each $\delta^{13}C_{carb}$ cycle in the microbialite with the $\delta^{13}C_{carb}$ records present in other sections, due to the difference in sampling resolution. At the coarse sampling resolution of the other sections, however, significant fluctuations in isotope composition are visible (Krull et al., 2004; Mu et al., 2009; Newton et al., 2004 and references therein), suggesting that the variability seen at Cili is of broader significance. The high-resolution $\delta^{13}C_{carb}$ record in the microbialite layer indicates that the carbon cycle after the main oceanic mass extinction was extremely unstable, and its correlation with $\delta^{34}S_{CAS}$ may reflect unstable redox conditions in the ocean.

5.2.2. $\delta^{34}S_{CAS}$

It is commonly thought that the Permian oceanic sulfate reservoir was characterized by low sulfur isotope composition, less than 15‰ (Claypool et al., 1980). However, the $\delta^{34}S_{CAS}$ during the P–Tr transition interval in this section is relatively high, as high as +27‰ (Fig. 3). The high sulfate sulfur isotope composition was also found in other sections. Kaiho et al. (2001) reported $\delta^{34}S_{CAS}$ as high as +30‰ at the Meishan section in South China, and this was confirmed by later work (Riccardi et al., 2006). The extracted carbonate-associated-sulfate from the western Tethyan Ocean also contains high values of $\delta^{34}S_{CAS}$; they are +25‰ to +27‰ in Siusi section (Newton et al., 2004), +23‰ in Bálvány section (Kaiho et al., 2006b), and +20‰ in Bulla section (Gorjan et al., 2007) (Fig. 6B). The high sulfur isotope compositions at these sections support our contention that the $\delta^{34}S_{CAS}$ values at the Cili section are primary, and most importantly, global.

The negative shift in $\delta^{34}S_{CAS}$ in the upper part of the skeletal limestone is also present in the Meishan section in South China (Riccardi et al., 2006), Siusi section and Bulla section in Italy (Gorjan et al., 2007; Newton et al., 2004) and Bálvány section in Hungary (Kaiho et al., 2006b) (Fig. 6B). The gradually increasing $\delta^{34}S_{CAS}$ spanning the main event level has also been recognized by others studying Tethyan sections (Gorjan et al., 2007; Kaiho et al., 2006b; Korte et al., 2004a; Newton et al., 2004) (Fig. 6B). The positive shift is consistent with the notion that increasing ocean anoxia (leading to enhanced pyrite burial) accompanied (caused?) the mass extinction.

Following the positive excursion spanning the main mass extinction boundary, a large decrease from +27‰ to +20‰ is documented in $\delta^{34}S_{CAS}$ at the base of the microbialite layer. Then $\delta^{34}S_{CAS}$ returns to +27‰, and remains relatively constant for the depth interval from 2 to 3.8 m. A second 10‰ decrease of $\delta^{34}S_{CAS}$ follows the positive plateau of the sulfur isotope compositions and terminates at the upper part of the microbialite layer, after which the $\delta^{34}S_{CAS}$ again increases. The double-dip pattern is essentially identical to that identified at the Siusi section, Bálvány section and Bulla section in Italy (Gorjan et al., 2007; Kaiho et al., 2006b; Newton et al., 2004). Because of the low-resolution of the $\delta^{34}S_{CAS}$ record in the Meishan section, it is impossible for us to compare the short-term trends in $\delta^{34}S_{CAS}$ between these two sections. The similar variation pattern observed in widely spaced sections infers a regional or global $\delta^{34}S_{CAS}$ record, which might be associated with changes in the extent of oceanic anoxia.

It is interesting to note that while the pattern of sulfur isotope variability is similar from location to location, the absolute $\delta^{34}S_{CAS}$ values vary geographically among the sections. While the $\delta^{34}S_{CAS}$ values in the Cili section center around +22‰, the corresponding data in the Siusi section, Meishan section, Bálvány section and Bulla section are +18‰, +20‰, +20‰ and +14‰, respectively (Fig. 6B). Diagenetic effects have been ruled out by the authors who studied these other sections and are thus unlikely to explain the geographic variations in $\delta^{34}S_{CAS}$. The influence of upwelling deepwater

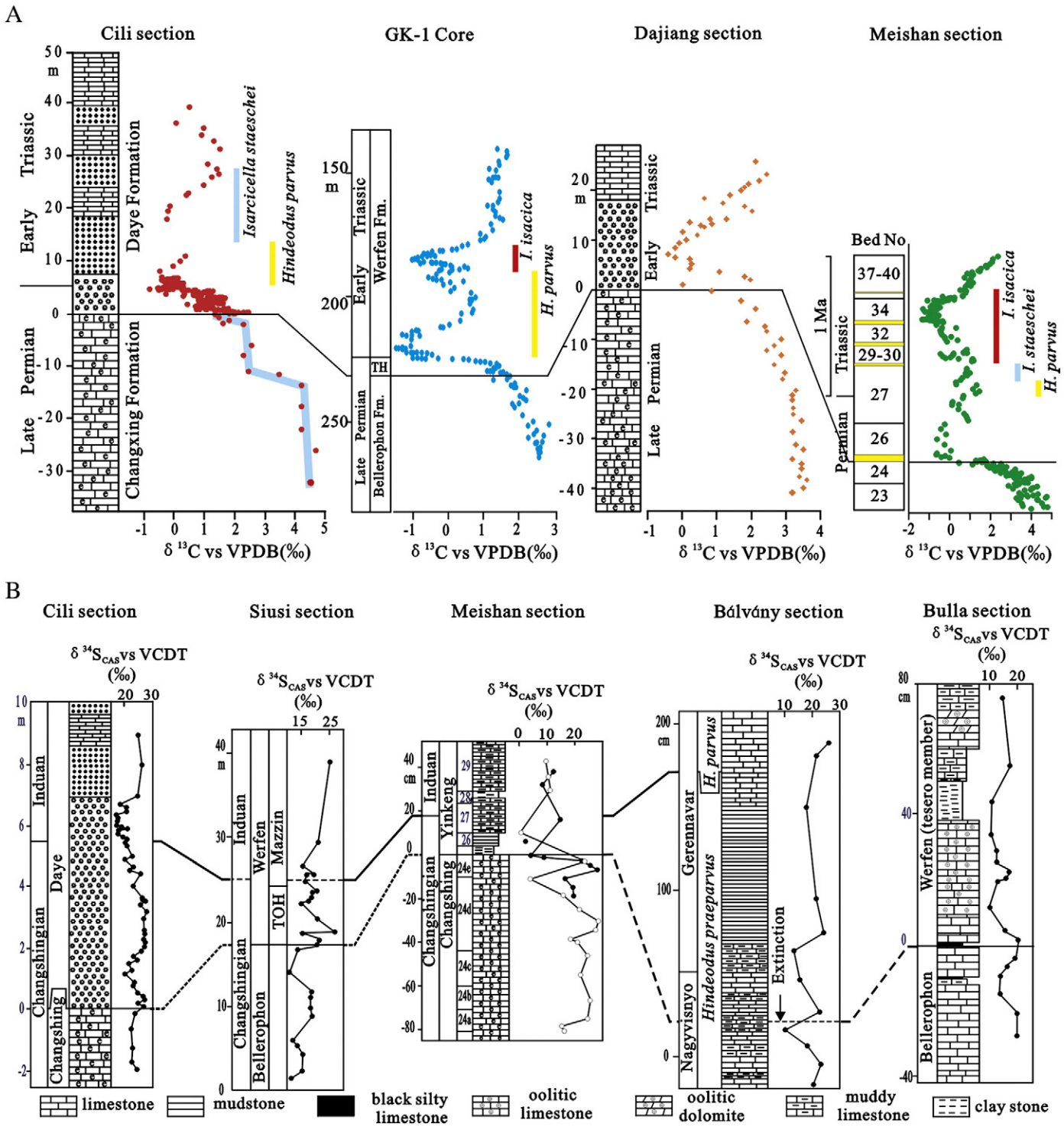

Fig. 6. A: Global comparison of the evolution of the carbonate carbon isotope compositions during the P–Tr transition. The line which connects all the sections represents the bottom of the event horizon which represents the mass extinction boundary. The conodont zones at GK-1 core and Meishan sections are after Jiang et al. (2007) and Schönlaub (1991), respectively. b: Global comparison of the sulfate sulfur isotope compositions during the P–Tr transition among different sections. The Siusi section is according to Newton et al. (2004), the Bulla section is according to Farabegoli et al. (2007) and Gorjan et al. (2007), the Meishan section is according to Kaiho et al. (2001) (Black points) and Riccardi et al. (2006) (Hollow points) and the Bálvány section is according to Kaiho et al. (2006b). The lower dashed line represents the bottom of the microbialite at the Cili section and their equivalent horizons of first mass extinction at other sections. The upper solid line at the Cili section and Siusi section represent the supposed P–Tr boundary as indicated by the first appearance of conodont *Hindeodus parvus*. The other lithologic legends in A and B are the same as Fig. 1 in text.

undoubtedly varied from place to place, but at least in South China, the expected differences are not observed. Affected by bacterial sulfate reduction, the sulfate sulfur isotope composition in deep water would be expected to be much heavier than that in shallow water. However, the heavier $\delta^{34}S_{CAS}$ in the shallow Cili section in comparison with that in the deeper Meishan section, likely more subject to upwelling, argues against variations in upwelling strength as an explanation for the spatial pattern of $\delta^{34}S_{CAS}$. Indeed, there is considerable variation among all the shallow sections (Gorjan et al., 2007; Kaiho et al., 2006b; Newton et al., 2004) that likely reflect varying rates of sulfate reduction in these (intermittently) anoxic basins. In any event, spatial variations in $\delta^{34}S_{CAS}$ are unlikely in an

ocean with near-modern sulfate concentrations, because the residence time of sulfate is considerably longer than the mixing time of the ocean. Instead, it suggests low oceanic sulfate concentrations, a condition that we explore in detail below.

5.3. Magnitude of $\delta^{34}S_{CAS}$ fluctuations

To determine whether the rate of isotope variation in the microbialite is anomalous we need to establish both the magnitude of variability and the duration of the event. The time from the main mass extinction horizon to the P–Tr boundary (indicated by the first appearance of the conodont *Hindeodus parvus*) at Meishan is suggested to be 0.5 Ma (Bowring et al., 1998; Jin et al., 2000), which is broadly consistent with the estimated duration in the Shangsi section (Mundil et al., 2004). The first appearance of the conodont *Hindeodus parvus* at the Cili section is located at 5.70 m above the base of the microbialite. Compared with the Meishan section, the time interval of microbialite deposition at the Cili section thus is about 0.6 Ma, if we suppose the sedimentation rate of the microbialite is constant. Sulfate sulfur isotope composition at the Cili section then indicates that the rate of the sulfur isotope variation is very large, as large as 7‰ in 100 ky. Rapid variation in $\delta^{34}S_{CAS}$ is also characteristic of other end-Permian sections around the Tethyan Ocean (Gorjan et al., 2007; Kaiho et al., 2001; Kaiho et al., 2006a; Newton et al., 2004; Riccardi et al., 2006) (Fig. 6B). These highly resolved, coherent, large amplitude and short duration $\delta^{34}S_{CAS}$ fluctuations indicate significant fluctuations in sulfur cycling, sensitively recorded by a marine sulfate reservoir with a response time that is shorter than that characteristic of the Cenozoic (Kump, 1989; Kurtz et al., 2003).

5.4. Test for coupled $\delta^{34}S_{CAS}$ and $\delta^{13}C_{carb}$ in the microbialite

The profile of $\delta^{13}C_{carb}$ and $\delta^{34}S_{CAS}$ at the Cili section suggests these two parameters are co-variant in the microbialite layer (Fig. 3B). A cross-plot of $\delta^{13}C_{carb}$ and $\delta^{34}S_{CAS}$ reveals that they are indeed highly positively correlated ($R^2 = 0.55$, $n = 45$, $p < 0.001$) (Fig. 7A). Cross correlation of $\delta^{13}C_{carb}$ and $\delta^{34}S_{CAS}$ shows that peak correlation occurs with no time delay (Fig. 7B). It is worth noting that the positive correlation between $\delta^{13}C_{carb}$ and $\delta^{34}S_{CAS}$ may also present in samples from the post-extinction Siusi section (West Tethys Ocean) as argued by Algeo et al. (2008) though at considerably lower resolution (Newton et al., 2004).

These results indicate comparably responsive global C and S reservoirs, quite unlike the general situation in the Phanerozoic, where the sulfur isotope variations lag, or on a 10^8-year timescale, vary inversely with those of carbon (Kump & Garrels, 1986; Veizer et al., 1980). Moreover, it varies rapidly (Fig. 3B), a phenomenon observed at other sections around the Tethyan Ocean (Fig. 6B), again indicating that the marine sulfate reservoir was small.

Upwelling of euxinic waters has been invoked to explain co-variation of carbon and sulfur isotope compositions in Late Permian boundary sections. As a result of organic matter regeneration and isotope fractionation during sulfate reduction, deep euxinic water masses have low $\delta^{13}C$ and low $\delta^{34}S$ in sulfide but elevated $\delta^{34}S$ in the sulfate. Upwelling of these deep waters into shallow water followed by pyrite and limestone precipitation could generate a negative shift in both $\delta^{34}S_{pyrite}$ and $\delta^{13}C_{carb}$, as hypothesized by Algeo et al. (2008). The positive correlation between $\delta^{13}C_{carb}$ and $\delta^{34}S_{CAS}$, shown in our record requires a different explanation. Upwelling of ^{34}S enriched sulfate would drive surface sulfate $\delta^{34}S$ in the positive direction while the inorganic carbon $\delta^{13}C$ would shift toward lower values. The upwelling deep water masses would thus induce negative excursion in $\delta^{13}C_{carb}$, but positive excursion in $\delta^{34}S_{CAS}$. Oxidation of some part of the hydrogen sulfide pool to sulfate would reduce the magnitude of the positive shift in $\delta^{34}S$ of the sulfate, but even with complete sulfide oxidation, the $\delta^{34}S$ of surface waters would simply return to their original value. Hence, the upwelling hypothesis appears not to apply to the post-extinction variations we observe at Cili.

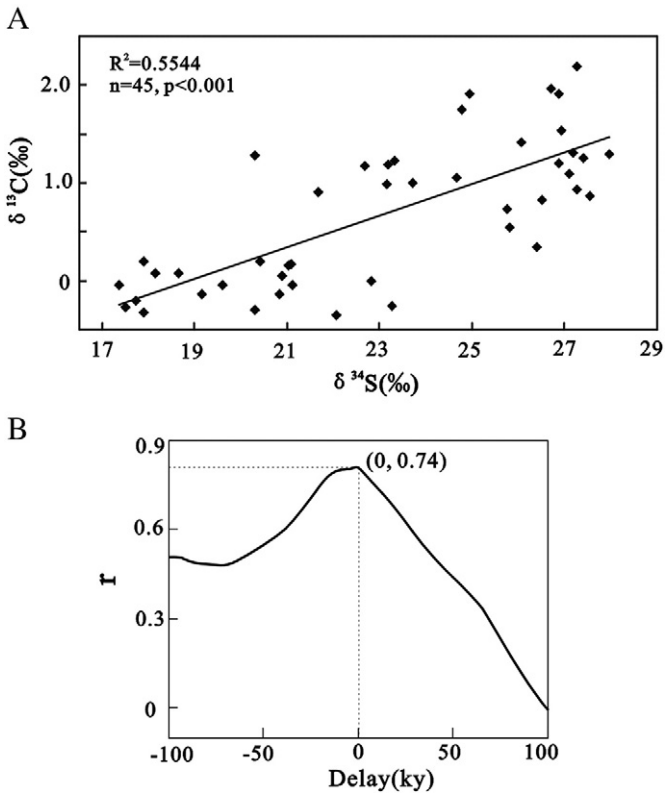

Fig. 7. A: Cross plot of $\delta^{13}C_{carb}$ and $\delta^{34}S_{CAS}$ in the microbialite interval at the Cili section. B: Cross correlation between $\delta^{13}C_{carb}$ and $\delta^{34}S_{CAS}$ with the data interpolated into every thousand years.

5.5. Numerical results

A box model of the global carbon and sulfur biogeochemical cycles is used here to investigate this coupling during the P–Tr crisis (see Supplementary Information). When calculating organic carbon burial rates from carbon isotope values and their derivatives, rapid decreases in $\delta^{13}C_{carb}$, as observed here, produce unphysical negative burial rates if a conventional long-term carbon cycle model that only treats the balance between weathering and burial fluxes (Kump & Garrels, 1986) is used. Such fluctuations instead may represent transfers of carbon from more labile reduced reservoirs within the ocean itself, e.g., from a large (relative to today) dissolved organic carbon (DOC) reservoir to the dissolved inorganic carbon (DIC) reservoir, as proposed to explain Neoproterozoic carbon isotope fluctuations (Rothman et al., 2003). We likewise suppose that during this potentially analogous time (Grotzinger & Knoll, 1995), the DOC reservoir size was large. In the Supplementary Informationy we show that satisfactory solutions can also be obtained with a smaller DOC reservoir and variable isotope fractionation. Alternatively, growth and shrinkage of a reactive surface sediment or marine methane clathrate reservoir could explain the rapid fluctuations (Berner, 2002). In the model, the observed carbon isotope record is used to drive variations in the rate of organic matter and DOC production (via productivity) and, ultimately, of organic carbon burial (presumed to be a constant fraction of the marine DOC reservoir size, as in Rothman et al., 2003). As the DOC reservoir size changes, so too does its rate of oxidation, which drives changes in the sulfate reduction rate, and thus in the size of the (euxinic) marine hydrogen sulfide reservoir. We thus couple the C and S cycles by specifying that a fixed proportion of the DOC oxidation flux arises from sulfate reduction. Variations in the rates of

sulfate reduction, sulfide oxidation and pyrite burial affect the size and the isotope composition of the marine sulfate reservoir. Values of marine $\delta^{34}S$ predicted in this way are then compared to the preserved $\delta^{34}S_{CAS}$ record (Fig. 8A).

We find that we can only approach a fit to the variability and trend of the $\delta^{34}S_{CAS}$ record with a substantial reduction in the marine sulfate reservoir size; at modern sulfate concentrations (29 mM) the model generates no significant variation on the timescale of our observations (Fig. 8A). If we specify a fixed sulfur isotope fractionation during sulfate reduction, a reasonable fit to the observations can only be obtained with an initial oceanic sulfate content less than or equal to 1×10^{18} mol, or a concentration of ~700 μM (Fig. 8A).

The simulated isotope record exhibits somewhat more variability than observed, suggesting that this reservoir size may be too small. Moreover, the amplitude of the simulated $\delta^{34}S_{CAS}$ is still less than the observed (Fig. 8A). In order to improve the model fit to the observed data, we allow the sulfur isotope fractionation to vary in a specified fashion, following the $\delta^{34}S_{CAS}$ records (Fig. 8B), with a somewhat larger initial reservoir size (6×10^{18} mol, or ~4 mM). The required variability in $\Delta^{34}S$ follows the $\delta^{34}S_{CAS}$ values, suggesting a coupling between fractionation and sulfate reduction rate. Hurtgen et al. (2009) noted that variation in $\Delta^{34}S$ could reflect the locus of sulfate reduction, particularly in an ocean with low sulfate concentration. Bacterial sulfate reduction occurring in the water column occurs in an open system with maximum possible $\Delta^{34}S$, whereas bacterial sulfate reduction occurring in the relatively closed sedimentary pore water system would generate a smaller net $\Delta^{34}S$. Thus, the stipulated co-variance between $\Delta^{34}S$ and $\delta^{34}S$ in our model results could be justified to be the result of water-column sulfate reduction and pyrite production during euxinic intervals in the shallow waters at Cili; elevated $\delta^{13}C$ and $\delta^{34}S$ would be the expected consequence of the associated high rates of sequestration of reduced sulfur and carbon. The specified variability in the fractionation factor (Fig. 8B) is similar in magnitude to the observed variations in isotope difference between preserved CAS and pyrite reported elsewhere (Gorjan et al., 2007).

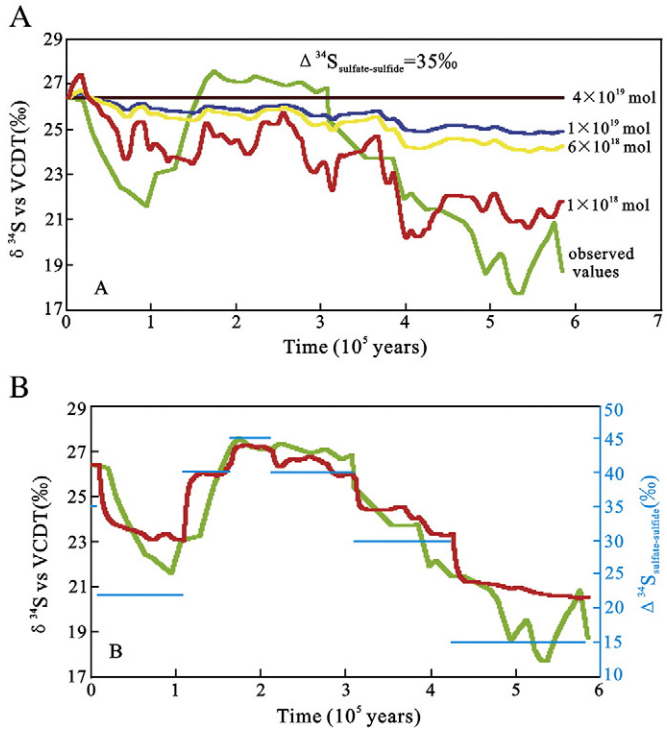

Fig. 8. Comparison between the observed (green) and simulated CAS-sulfur isotope composition with different assumed initial oceanic sulfate concentrations and sulfur isotope fractionation. (A) Simulated sulfur isotope compositions with constant sulfur isotope fractionation = 35‰ and different initial oceanic sulfate content. (B) Observed (green) and simulated sulfur isotope composition (red) with variable sulfur isotope fractionation (shown as horizontal bars) and initial oceanic sulfate content = 6×10^{18} mol.

Sensitivity analysis indicates that the fundamental result (that a small oceanic sulfate reservoir size is needed to fit the co-variations in carbon and sulfur isotopes) is robust despite significant uncertainties in the model parameters (see Supplementary Information).

The analysis and interpretation of brine inclusions in halite indicate that the oceanic sulfate concentration has varied greatly in the Phanerozoic, with a distinct decline from Late Permian to Middle Triassic (Kovalevych et al., 2002). Based on these data, the oceanic sulfate concentration was calculated to be about 20 mM in the Late Permian (Horita et al., 2002; Lowenstein et al., 2005), considerably higher than we propose for the latest Permian. However, there is a lack of evaporite data from the P–Tr crisis interval and from much of the Early Triassic against which to evaluate our hypothesis. Moreover, the brine-inclusion calculations suffer from being non-unique: to solve for both Ca^{2+} and SO_4^{2-} concentrations, these investigators need to assume a concentration product of the two ions. Thus, a rapid depletion of sulfate concentration in the late Permian–early Triassic is certainly reasonable and not inconsistent with the data at hand. Furthermore, our conclusion about low oceanic sulfate concentration is consistent with the qualitative interpretation by others that the oceanic sulfate concentration declined substantially in Late Permian and Early Triassic (Holser & Magaritz, 1987; Marenco et al., 2008).

5.6. Mechanisms inducing low oceanic sulfate concentration

The Late Permian, prior to the extinction event, was a time of voluminous gypsum evaporite deposition (Zharkov, 1984). Putting quantitative estimates on evaporite sulfate drawdown based on the preserved evaporite record is fraught with uncertainties. However, using the Hay et al. (2006) estimates for Late Permian halite extraction (5.3×10^{18} kg) and typical gypsum/halite ratio of 1:4 yields a total mass of extracted gypsum 1.3×10^{18} kg. Using the molecular weight of gypsum (172 g/mol) leads to an estimated 8.4×10^{18} mol of SO_4^{2-} extracted, or approximately a 6 mM reduction in the seawater sulfate concentration. This is likely a conservative estimate, because the gypsum/halite ratio of Permian evaporites is considered unusually high (Zharkov, 1984), and much of the preserved sulfate evaporite is anhydrite, with a smaller molecular weight. Interestingly, low oceanic sulfate concentrations inferred for the Early Cretaceous also followed periods characterized by voluminous preserved evaporites (Wortmann & Chernyavsky, 2007).

Other lines of argument support our contention that Late Permian seawater was severely depleted in sulfate. Enhanced euxinia prior to the main mass extinction at Meishan section in South China (Cao et al., 2009; Grice et al., 2005) and elsewhere (Algeo et al., 2007; Hays et al., 2007; Nabbefeld et al., in press) presumably reflects the intensification of bacterial sulfate reduction, which could significantly reduce the oceanic sulfate concentration if it were already depleted by evaporite deposition. Moreover, with the onset of anoxia, sulfate concentrations may have dropped even further, an expected consequence of a collapse of bioturbation during oceanic anoxic/euxinic intervals, as recently argued by Canfield and Farquhar (2009). Thus we suggest that marine sulfate concentrations fell throughout the Late Permian, reaching critically low levels in the latest Permian.

5.7. Effects on the mass extinction

The substantial time lag (~1.5 million years) observed between the establishment of photic zone euxinia and the main mass extinction in the Meishan sections (Cao et al., 2009) argues against euxinia alone as the main mechanism of mass extinction (Knoll et al., 2007; Kump et al., 2005; Wignall, 2007). Clearly there seems to be a

triggering associated with contemporaneous volcanism (Svensen et al., 2009). But might low sulfate concentrations have contributed to the stresses that marine and terrestrial organisms faced in the lead-up to the end-Permian mass extinction?

In the modern ocean, anaerobic oxidation by sulfate is a major sink for methane (D'Hondt et al., 2002; Valentine, 2002). Thus, the loss of the two major oxidants in seawater (oxygen and sulfate) would tend to promote methanogenesis in sulfate-depleted marine pore waters, eliminate anaerobic CH_4 oxidation as a major methane sink, and allow for the accumulation of CH_4 in the ocean and release to the atmosphere. The resulting increased atmospheric concentration of methane, which is a strong greenhouse gas, could enhance warming and further reduce oxygen solubility in the ocean.

Considering that the low oceanic sulfate concentration could not occur instantaneously, relatively low oceanic sulfate concentration would be present directly below the base of the microbialite. Fossils records suggest that the end-Permian biotic crisis might have started before the distinct extinction horizon (Powers and Bottjer, 2007). Jin et al. (2000) demonstrated that some species disappear gradually in the strata below the main oceanic mass extinction in the Meishan section. Yang et al. (1991) and Yin et al. (2007) proposed a prelude of the mass extinction (bed 24e) in the Meishan section. Recently, Song et al. (2009) show that some foraminiferal species disappear in the strata below the base of the microbialite in the Dajiang section in the Great Guizhou Bank. The temporal relationship hints that the biotic stressors existed prior to the main mass extinction may relate to lower oceanic sulfate concentration and its consequence. Volcanism and its effects on climate and atmospheric chemistry might then have been the final blow to a marine and terrestrial biota already highly stressed by extreme global warming and anoxic, high CO_2 and high H_2S marine waters.

6. Conclusions

High-resolution carbonate carbon and carbonate-associated sulfate–sulfur isotope measurements of the Cili microbialite section suggest strongly coupled carbon and sulfur cycling during the P–Tr transitional interval. Widespread, large amplitude variations in $\delta^{34}S_{CAS}$ seem to require a small oceanic sulfate reservoir during the P–Tr transition. A simple coupled non-steady-state C–S box model indicates the oceanic sulfate concentration could have been less than 1 mM, or 3% of the modern oceanic sulfate concentration. The low oceanic sulfate concentration may have been the result of both voluminous gypsum evaporite deposition in the Early to Middle Permian and further depletion as the ocean became anoxic and pyrite burial increased. The substantial decline in oceanic sulfate concentration may have amplified global warming through promoting methanogenesis. Although it is not likely to be the primary kill mechanism for the end-Permian mass extinction, low oceanic sulfate concentrations may have exacerbated the existing inimical conditions, perhaps beyond the limit of survivability.

Acknowledgments

The authors would like to thank Prof. Chaoyong Hu, Dr. Xiaoyan Ruan and Shouzhi Hu for their assistance in the field. We are indebted to Prof. Tom Algeo and Ying Cui for discussion of P–Tr events, and Prof. Shuhai Xiao for constructive suggestions and critical comments on an earlier version of the manuscript. Master's students Xiao Bai, Lei He, Ze Zhang, Xia Wu and Huan Wang are also thanked for their help in the laboratory. This work was supported by the Chinese National Natural Science Foundation (grant nos. 40730209 and 40921062), the 973 program (grant no. 2011CB808800), the 111 project (grant no. B08030), the US National Science Foundation (EAR 0807744 to LRK), and the US NASA Astrobiology Institute (grant no. NAA09DA76A) to MAA and LRK.

Appendix A. Supplementary data

Supplementary data to this article can be found online at doi:10.1016/j.epsl.2010.09.041.

References

Algeo, T.J., Ellwood, B., Nguyen, T.K.T., Rowe, H., Maynard, J.B., 2007. The Permian–Triassic boundary at Nhi Tao, Vietnam: evidence for recurrent influx of sulfidic watermasses to a shallow-marine carbonate platform. Palaeogeogr. Palaeoclimatol. Palaeoecol. 252, 304–327.

Algeo, T.J., Shen, Y.A., Zhang, T.G., Lyons, T.W., Bates, S., Rowe, H., Nguyen, T.K.T., 2008. Association of ^{34}S-depleted pyrite layers with negative carbonate $\delta^{13}C$ excursions at the Permian–Triassic boundary: evidence for upwelling of sulfidic deep-ocean water masses. Geochem. Geophys. Geosyst. 9, Q04025 10.1029/2007GC001823.

Basu, A.R., Petaev, M.I., Poreda, R.J., Jacobsen, S.B., Becker, L., 2003. Chondritic meteorite fragments associated with the Permian–Triassic boundary in Antarctica. Science 302, 1388–1392.

Baud, A., Magaritz, M., Holser, W.T., 1989. Permian–Triassic of the Tethys: carbon isotope studies. Geol. Rundsch. 78, 649–677.

Baud, A., Richoz, S., Pruss, S., 2007. The lower Triassic anachronistic carbonate facies in space and time. Glob. Planet. Change 55, 81–89.

Berner, R.A., 2002. Examination of hypotheses for the Permo-Triassic boundary extinction by carbon cycle modeling. Proc. Natl Acad. Sci. USA 99, 4172–4177.

Bowring, S.A., Erwin, D.H., Jin, Y.G., Martin, M.W., Davidek, K., Wang, W., 1998. U/Pb zircon geochronology and tempo of the end-Permian mass extinction. Science 280, 1039–1045.

Canfield, D.E., Farquhar, J., 2009. Animal evolution, bioturbation, and the sulfate concentration of the oceans. Proc. Natl Acad. Sci. USA 106, 8123–8127.

Cao, C.Q., Wang, W., Jin, Y.G., 2002. The change of carbon isotope during the Permian–Triassic boundary in Meishan, Zhejiang province. Chin. Sci. Bull. 47, 302–306.

Cao, C.Q., Love, G.D., Hays, L.E., Wang, W., Shen, S.Z., Summons, R.E., 2009. Biogeochemical evidence for euxinic oceans and ecological disturbance presaging the end-Permian mass extinction event. Earth Planet. Sci. Lett. 281, 188–201.

Claypool, G.E., Holser, W.T., Kaplan, I.R., Sakai, H., Zak, I., 1980. The age curves of sulfur and oxygen isotopes in marine sulfate and their mutual interpretation. Chem. Geol. 28, 199–260.

Corsetti, F.A., Baud, A., Marenco, P.J., Richoz, S., 2005. Summary of Early Triassic carbon isotope records. C. R. Palevol. 4, 473–486.

D'Hondt, S., Rutherford, S., Spivack, A.J., 2002. Metabolic activity of subsurface life in deep-sea sediments. Science 295, 2067–2070.

Dolenec, T., Ogorelec, B., Dolenec, M., Lojen, S., 2004. Carbon isotope variability and sedimentology of the Upper Permian carbonate rocks and changes across the Permian–Triassic boundary in the Masore section (Western Slovenia). Facies 50, 287–299.

Erwin, D.H., 2006. Extinction: how life on earth nearly ended 250 million years ago. Princeton University press, New York.

Farabegoli, E., Perri, M.C., Posenato, R., 2007. Environmental and biotic changes across the Permian–Triassic boundary in western Tethys: the Bulla parastratotype, Italy. Glob. Planet. Change 55, 109–135.

Feng, Z.Z., Yang, Y.Q., Jin, Z.K., Li, S.W., Bao, Z.D., 1997. Lithofacies palaeogeography of Permian of South China. Petroleum University Press, Beijing. 1-242 pp. (in Chinese).

Gorjan, P., Kaiho, K., Kakegawa, T., Niitsuma, S., Chen, Z.Q., Kajiwara, Y., Nicora, A., 2007. Paleoredox, biotic and sulfur-isotope changes associated with the end-Permian mass extinction in the western Tethys. Chem. Geol. 244, 483–492.

Grice, K., Cao, C.Q., Love, G.D., Böttcher, M.E., Twitchett, R.J., Grosjean, E., Summons, R.E., Turgeon, S.C., Dunning, W., Jin, Y.G., 2005. Photic zone euxinia during the Permian–Triassic superanoxic event. Science 307, 706–709.

Grotzinger, J.P., Knoll, A.H., 1995. Anomalous carbonate precipitates: is the Precambrian the key to the Permian? Palaios 10, 578–596.

Hay, W.W., Migdisov, A., Balukhovsky, A.N., Wold, C.N., Flogel, S., Soding, E., 2006. Evaporites and the salinity of the ocean during the Phanerozoic: implications for climate, ocean circulation and life. Palaeogeogr. Palaeoclimatol. Palaeoecol. 240, 3–46.

Hays, L.E., Beatty, T., Henderson, C.M., Love, G.D., Summons, R.E., 2007. Evidence for photic zone euxinia through the end-Permian mass extinction in the Panthalassic Ocean (Peace River Basin, Western Canada). Palaeoworld 16, 39–50.

Holser, W.T., Magaritz, M., 1987. Events near the Permian–Triassic boundary. Mod. Geol. 11, 155–180.

Holser, W.T., Schonlaub, H.P., Attrep Jr., M., Boeckelmann, K., Klein, P., Magaritz, M., Orth, C.J., Fenninger, A., Jenny, C., Kralik, M., Mauritsch, H., Pak, E., Schramm, J.M., Stattegger, K., Schmoller, R., 1989. A unique geochemical record at the Permian–Triassic boundary. Nature 337, 39–44.

Horita, J., Zimmermann, H., Holland, H.D., 2002. Chemical evolution of seawater during the Phanerozoic: implications from the record of marine evaporites. Geochim. Cosmochim. Acta 66, 3733–3756.

Hurtgen, M.T., Pruss, S.B., Knoll, A.H., 2009. Evaluating the relationship between the carbon and sulfur cycles in the later Cambrian ocean: an example from the Port au Port Group, western Newfoundland, Canada. Earth Planet. Sci. Lett. 281, 288–297.

Jiang, H.S., Lai, X.L., Luo, G.M., Aldridge, R.J., Zhang, K.X., Wignall, P.B., 2007. Restudy of conodont zonation and evolution across the Permian–Triassic Boundary at Meishan Section, Changxing, Zhejiang. Glob. Planet. Change 55, 39–55.

Jin, Y.G., Wang, Y., Wang, W., Shang, Q.H., Cao, C.Q., Erwin, D.H., 2000. Pattern of marine mass extinction near the Permian–Triassic boundary in south China. Science 289, 432–436.
Kaiho, K., Chen, Z.Q., Kawahata, H., Kajiwara, Y., Sato, H., 2006a. Close-up of the end-Permian mass extinction horizon recorded in the Meishan section, South China: sedimentary, elemental, and biotic characterization and a negative shift of sulfate sulfur isotope ratio. Palaeogeogr. Palaeoclimatol. Palaeoecol. 239, 396–405.
Kaiho, K., Kajiwara, Y., Chen, Z.Q., Gorjan, P., 2006b. A sulfur isotope event at the end of the Permian. Chem. Geol. 235, 33–47.
Kaiho, K., Kajiwara, Y., Nakano, T., Miura, Y., Kawahata, H., Tazaki, K., Ueshima, M., Chen, Z.Q., Shi, G.R., 2001. End Permian catastrophe by a bolide impact: evidence of a gigantic release of sulfur from the mantle. Geology 29, 815–818.
Kaufman, A.J., Knoll, A.H., 1995. Neoproterozoic variations in the C isotopic composition of seawater: stratigraphic and biogeochemical implications. Precambrian Res. 73, 27–49.
Knoll, A.H., Bambach, R.K., Payne, J.L., Pruss, S.B., Fischer, F., 2007. Paleophysiology and end-Permian mass extinction. Earth Planet. Sci. Lett. 256, 295–313.
Korte, C., Kozur, H.W., Joachimski, M.M., Strauss, H., Veizer, J., Schwark, L., 2004a. Carbon, sulfur, oxygen and strontium isotope records, organic geochemistry and biostratigraphy across the Permian/Triassic boundary in Abadeh, Iran. Int. J. Earth Sci. 93, 565–581.
Korte, C., Kozur, H.W., Mohtat-Aghai, P., 2004b. Dzhulfian to lowermost Triassic δ13C record at the Permian/Triassic boundary section at Shahreza, Central Iran. Hallesches Jb. Geowiss. Reihe B 18, 73–78.
Korte, C., Kozur, H.W., 2010. Carbon isotope stratigraphy across the Permian–Triassic boundary: a review. J. Asian Earth Sci. 39, 215–235.
Korte, C., Pande, P., Kalia, P., Kozur, H., Joachimski, M.M., Oberhansli, H., 2010. Massive volcanism at the Permian–Triassic boundary and its impact on the isotopic composition of the ocean and atmosphere. J. Asian Earth Sci. 37, 293–311.
Kovalevich, V.M., Marek, P.T., Petrichenko, O.I., 1998. Secular variation in seawater chemistry during the Phanerozoic as indicated by brine inclusions in halite. J. Geol. 106, 695–712.
Kovalevych, V., Peryt, T.M., Beer, W., Geluk, M., Halas, S., 2002. Geochemistry of Early Triassic seawater as indicated by study of the Rot halite in the Netherlands, Germany, and Poland. Chem. Geol. 182, 549–563.
Krull, E.S., Lehrmann, D.J., Druke, D., Kessel, B., Yu, Y.Y., Li, R.X., 2004. Stable carbon isotope stratigraphy across the Permian–Triassic boundary in shallow marine carbonate platforms, Nanpanjiang Basin, south China. Palaeogeogr. Palaeoclimatol. Palaeoecol. 204, 297–315.
Kump, L.R., 1989. Alternative modeling approaches to the geochemical cycles of carbon, sulfur, and strontium isotopes. Am. J. Sci. 289, 390–410.
Kump, L.R., Garrels, R.M., 1986. Modeling atmospheric O-2 in the global sedimentary redox cycle. Am. J. Sci. 286, 337–360.
Kump, L.R., Pavlov, A., Arthur, M.A., 2005. Massive release of hydrogen sulfide to the surface ocean and atmosphere during interval of oceanic anoxia. Geology 33, 397–400.
Kurtz, A.C., Kump, L.R., Arthur, M.A., Zachos, J.C., Paytan, A., 2003. Early Cenozoic decoupling of the global carbon and sulfur cycles. Paleoceanography 18. doi:10.1029/2003PA000908.
Lehrmann, D.J., Payne, J.L., Felix, S.V., Dillett, P.M., Wang, H.M., Yu, Y.Y., Wei, J.Y., 2003. Permian–Triassic boundary sections from shallow-marine carbonate platforms of the Nanpanjiang Basin, South China: implications for oceanic conditions associated with the End-Permian extinction and its aftermath. Palaios 18, 138–152.
Liu, Y.S., Zong, K.Q., Kelemen, P.B., Gao, S., 2008. Geochemistry and magmatic history of eclogites and ultramafic rocks from the Chinese continental scientific drill hole: subduction and ultrahigh-pressure metamorphism of lower crustal cumulates. Chem. Geol. 247, 133–153.
Lowenstein, T.K., Timofeeff, M.N., Kovalevych, V.M., Horita, J., 2005. The major-ion composition of Permian seawater. Geochim. Cosmochim. Acta 69, 1701–1719.
Luo, G.M., Huang, J.H., Xie, S.C., Wignall, P.B., Tang, X.Y., Huang, X.Y., Yin, H.F., 2010. Relationships between carbon isotope evolution and variation of biota during the Permian–Triassic transition at Meishan Section, South China. Int. J. Earth Sci. 99, 775–784.
Magaritz, M., Bär, R., Baud, A., Holser, W.T., 1988. The carbon-isotope shift at the Permian–Triassic boundary in the southern Alps is gradual. Nature 331, 337–339.
Marenco, P.J., Corsetti, F.A., Hammond, D.E., Kaufman, A.J., Bottjer, D.J., 2007. Oxidation of pyrite during extraction of carbonate associated sulfate. Chem. Geol. 247, 124–132.
Marenco, P.J., Corsetti, F.A., Kaufman, A.J., Bottjer, D.J., 2008. Environmental and diagenetic variations in carbonate associated sulfate: an investigation of CAS in the Lower Triassic of the western USA. Geochim. Cosmochim. Acta 72, 1570–1582.
Mazumdar, A., Goldberg, T., Strauss, H., 2008. Abiotic oxidation of pyrite by Fe (III) in acidic media and its implications for sulfur isotope measurements of lattice bound sulfate in sediments. Chem. Geol. 253, 30–37.
McCrea, J.M., 1950. The isotopic chemistry of carbonates and a paleotemperature scale. J. Chem. Phys. 18, 849–857.
Mu, X.N., Kershaw, S., Li, Y., Guo, L., Qi, Y.P., Reynolds, A., 2009. High-resolution carbon isotope changes in the Permian–Triassic boundary interval, Chongqing, South China: implications for control and growth of earliest Triassic microbialites. J. Asian Earth Sci. 36, 434–441.
Mundil, R., Ludwig, K.R., Metcalfe, I., Renne, P.R., 2004. Age and timing of the Permian mass extinction: U/Pb dating of closed-system zircon. Science 305, 1760–1763.
Nabbefeld, B., Grice, K., Twitchett, R.J., Summons, R.E., Hays, L.E., Bottcher, M.E., Asif, M., in press. An integrated biomarker, isotopic and palaeoenvironmental study through the Late Permian event at Lusitaniadalen, Spitsbergen. Earth and Planetary Science Letters.
Newton, R.J., Pevitt, E.L., Wignall, P.B., Bottrell, S.H., 2004. Large shifts in the isotopic composition of seawater sulfate across the Permian–Triassic boundary in northern Italy. Earth Planet. Sci. Lett. 218, 331–345.
Payne, J.L., Lehrmann, D.J., Wei, J.Y., Orchard, M.J., Schrag, D.P., Knoll, A.H., 2004. Large perturbations of the carbon cycle during recovery from the End-Permian extinction. Science 305, 506–509.
Payne, J.L., Kump, L.R., 2007. Evidence for recurrent Early Triassic massive volcanism from quantitative interpretation of carbon isotope fluctuations. Earth Planet. Sci. Lett. 256, 264–277.
Powers, C.M., Bottjer, D.J., 2007. Bryozoan paleoecology indicates mid-Phanerozoic extinctions were the product of long-term environmental stress. Geology 35, 995–998.
Pruss, S.B., Bottjer, D.J., Corsetti, F.A., Baud, A., 2006. A global marine sedimentary response to the end-Permian mass extinction: examples from southern Turkey and the western United States. Earth Sci. Rev. 78, 193–206.
Reichow, M.K., Pringle, M.S., Al'Mukhamedov, A.I., Allen, M.B., Andreichev, V.L., Buslov, M.M., Davies, C.E., Fedoseev, G.S., Fitton, J.G., Inger, S., Medvedev, A.Y., Mitchell, C., Puchkov, V.N., Safonova, I.Y., Scott, R.A., Saunders, A.D., 2009. The timing and extent of the eruption of the Siberian Traps large igneous province: implications for the end-Permian environmental crisis. Earth Planet. Sci. Lett. 277, 9–20.
Riccardi, A.L., Arthur, M.A., Kump, L.R., 2006. Sulfur isotopic evidence for chemocline upward excursions during the end-Permian mass extinction. Geochim. Cosmochim. Acta 70, 5740–5752.
Richoz, S., Krystyn, L., Baud, A., Brandner, R., Horacek, M., Mohtat-Aghai, P., 2010. Permian–Triassic boundary interval in the Middle East (Iran and N. Oman): progressive environmental change from detailed carbonate carbon isotope marine curve and sedimentary evolution. J. Asian Earth Sci. 39, 236–253.
Rothman, D.H., Hayes, J.M., Summons, R.E., 2003. Dynamics of the Neoproterozoic carbon cycle. Proc. Natl Acad. Sci. USA 100, 8124–8129.
Schönlaub, H.P., 1991. The Permian–Triassic of the Gartnerkofel-1 core (Carnic Alps, Austria): conodont biostratigraphy. In: Holser, W.T., Schönlaub, H.P. (Eds.), The Permian–Triassic boundary in the Carnic Alps of Austria (Gartnerkofel region). Abhandlungen der Geologische Bundesanstalt, pp. 79–98.
Song, H.J., Tong, J.N., Chen, Z.Q., Yang, H., Wang, Y.B., 2009. End-Permian mass extinction of foraminifers in the Nanpanjiang Basin, South China. J. Paleontol. 83, 718–738.
Svensen, H., Planke, S., Polozov, A.G., Schmidbauer, N., Corfu, F., Podladchikov, Y.Y., Jamtveit, B., 2009. Siberian gas venting and the end-Permian environmental crisis. Earth and Planetary Science Letters 277, 490-500.
Valentine, D.L., 2002. Biogeochemistry and microbial ecology of methane oxidation in anoxic environments: a review. Antonie Leeuwenhoek 81, 271–282.
Veizer, J., Holser, W.T., Wilgus, C.K., 1980. Correlation of $^{13}C/^{12}C$ and $^{34}S/^{32}S$ secular variations. Geochim. Cosmochim. Acta 44, 579–587.
Wang, Q.X., Tong, J.N., Song, H.J., Yang, H., 2009. Evolution of the ecosystem across the Permian–Triassic boundary at the Kangjiaping Section in Cili, Hunan Province. Sci. China D 52, 797–806.
Wang, Y.B., Tong, J.N., Wang, J.S., Zhou, X.G., 2005. Calcimicrobialite after end-Permian mass extinction in South China and its palaeoenvironmental significance. Chin. Sci. Bull. 50, 665–671.
Ward, P.D., Botha, J., Buick, R., De Kock, M.O., Erwin, D.H., Garrison, G.H., Kirschvink, J.L., Smith, R., 2005. Abrupt and gradual extinction among Late Permian land vertebrates in the Karoo Basin, South Africa. Science 307, 709–715.
Wignall, P.B., 2007. The End-Permian mass extinction—how bad did it get? Geobiology 5, 303–309.
Wignall, P.B., Hallam, A., 1993. Gresbachian (earliest Triassic) palaeoenvironmental changes in the Salt Range, Pakistan and South China and their bearing on the Permo-Triassic mass extinction. Palaeogeography, Palaeoclimatology, Palaeoecology 102, 215–237.
Wortmann, U.G., Chernyavsky, B.M., 2007. Effect of evaporite deposition on Early Cretaceous carbon and sulfur cycling. Nature 446, 654–656.
Xie, S.C., Pancost, R.D., Huang, J.H., Wignall, P.B., Yu, J.X., Tang, X.Y., Chen, L., Huang, X.Y., Lai, X.L., 2007. Changes in the global carbon cycle occurred as two episodes during the Permian–Triassic crisis. Geology 35, 1083–1086.
Yang, H., Zhang, S.X., Jiang, H.S., Wang, Y.B., 2006. Age and general characteristics of the calcimicrobialite near the Permian–Triassic boundary in Chongyang, Hubei Province. J. China Univ. Geosci. 17, 121–125.
Yang, Z.Y., Wu, S.B., Yin, H.F., Xu, G.R., Zhang, K.X., Bi, X.M., 1991. Permo-Triassic events of South China: Beijing. Geological Publishing House, pp. 35–64 (in Chinese).
Yin, H.F., Feng, Q.L., Lai, X.L., Baud, A., Tong, J.N., 2007. The protracted Permo-Triassic crisis and the multi-episode mass extinction around the Permian–Triassic boundary. Glob. Planet. Changes 55, 1–20.
Zharkov, M.A., 1984. Paleozoic Slat Bearing Formations of the World. Springer, Berlin.